Molecular Insights into Caprock Integrity of Subsurface Hydrogen Storage: Perspective on Hydrogen-induced Swelling and Mechanical Response

Mehdi Ghasemi,*,[†] Mohamad Ali Ghafari,[‡] Masoud Babaei,*,[†] and Valentina Erastova*,[¶]

[†]Department of Chemical Engineering, The University of Manchester, Manchester M13 9PL, United Kingdom

[‡]Independent Researcher, Tehran, Iran

[¶]School of Chemistry, University of Edinburgh, Joseph Black Building, David Brewster Road, Edinburgh, EH9 3FJ, United Kingdom

E-mail: mehdi.ghasemi@manchester.ac.uk; masoud.babaei@manchester.ac.uk; valentina.erastova@ed.ac.uk

1

Abstract

The geological storage of hydrogen (H_2) requires reliable long-term caprock sealing, yet the nanoscale interactions between H_2 and clay minerals remain critically under-explored despite their importance for storage security. This lack of understanding has limited the ability to predict mechanical stability and leakage risks in H_2 storage formations. Using molecular simulations, this study investigates the swelling behavior and mechanical properties of sodium montmorillonite (Mt), a common smectite clay, under varying hydration states and interlayer H_2 contents. Results show that H_2 accelerates hydration-state transitions, narrows the stability window of crystalline swelling, and promotes asymmetric plume formation in confined interlayers. H_2 alters cation and water coordination, thereby weakening Na^+–Mt electrostatic interactions and modulating H-bond networks at the interface and in the bulk. Mechanical analysis reveals pronounced anisotropy in Mt. In-plane stiffness is mainly governed by basal spacing expansion, whereas out-of-plane stiffness is highly sensitive to the initial presence of water or H_2, which weaken interlayer cohesion. Tensile and compressive strengths in the in-plane directions follow in-plane stiffness trends, while the out-of-plane tensile strength is governed by Mt–water H-bonds. The presence of H_2 further promotes Mt sheets separation by disrupting nanoscale liquid bridges. Collectively, these results provide the first atomistic-scale evidence that intercalated H_2 reshapes swelling energetics, elastic anisotropy, and failure pathways in Mt, highlighting critical nanoscale mechanisms that may compromise caprock integrity during underground H_2 storage.

Introduction

Storage of hydrogen, H_2, at gigatonne capacities will form a central pillar of future sustainable energy systems, simultaneously mitigating CO_2 emissions and enabling the seasonal availability of green energy.[1,2] As the global energy landscape transitions toward carbon neutrality, large-scale geological storage of H_2 will be essential for maintaining the resilience, reliability, and adaptability of renewable energy infrastructures.[3] While underground H_2 storage (UHS) stands as the most economically efficient solution for large-scale energy storage, persistent and complex challenges associated with long-term storage efficacy continue to overshadow its technological maturity compared to other storage systems, currently limiting the progress of UHS development.[4,5]

In this context, the failure of caprock sealing is a significant concern.[6] Among the clay minerals in caprock, montmorillonite (Mt), with its unique properties including low permeability, high surface area, and swelling capacity, is a critical dual-role player, capable of enhancing sealing performance while also posing risks to caprock stability.[7] On one hand, Mt, like other clay minerals, can enhance caprock performance by forming dense, compact layers that act as effective seals, preventing fluid migration, with its fine-grained structure and fluid retention abilities further contributing to sealing efficiency.[8,9] However, on the other hand, these same properties can also negatively impact caprock stability under certain conditions. The high surface area of Mt facilitates processes such as ion exchange or gas intercalation, enhancing their interactions with fluids and making them susceptible to geomechanical and geochemical alterations, including structural changes and dissolution.[10,11]

The unique physical properties of H_2, such as its high diffusivity and lower density compared to CO_2, make it more likely to migrate toward the surface at a faster rate. Given these properties, H_2 should be stored deeper and in lower-permeability sites than CO_2 and CH_4 to ensure caprock confinement and prevent leakage. Our previous research revealed that H_2 can penetrate sub-nanopores as small as 0.5 nm in clay minerals, facilitated by its exceptional rotational flexibility compared to cushion gases like CO_2.[12] H_2 molecules intercalated in

clay-rich, water-saturated caprocks may become trapped due to H_2's low solubility in water and the presence of complex, disconnected pore pathways. This raises a key question: how does trapped H_2 impact the caprock's geomechanical properties, such as structural integrity, deformation, and long-term sealing?

To address this question, we focused on the swelling behavior of Mt, induced by H_2, and its subsequent impact on the geomechanical response. The swelling behavior of Mt has been extensively studied due to its sensitivity to hydration. Swelling proceeds via two primary mechanisms: (i) crystalline swelling, involving discrete interlayer water adsorption, and (ii) osmotic swelling at higher water uptake. Crystalline swelling occurs in stepwise transitions as water content increases, shifting from the dry state to a monolayer (0W → 1W), and subsequently to a bilayer hydration state (1W → 2W).[13,14] These transitions are typically identified through changes in the basal spacing (d_{001}), which reflect interlayer expansion. While there is a well-established understanding of how CO_2 intercalates into clay minerals and its effects on swelling and mechanical properties,[11,15–17] the unique physical properties of H_2 raise concerns about the direct applicability and transferability of CO_2-based knowledge to H_2 storage. These differences challenge the assumption that existing models and findings related to CO_2 storage can be fully adopted for H_2 storage.[12]

This study

In this study, we focus on the fundamental mechanism of H_2-induced swelling in Mt and perform comprehensive molecular-level simulations to investigate the impact of intercalated H_2 under caprock-relevant thermodynamic conditions. Specifically, we examine how H_2 intercalation affects the structural evolution and alters the mechanical behavior and macroscopic properties of the clay matrix. In doing so, we investigate the impact of interlayer-trapped H_2 on Mt swelling under varying hydration states (1W and 2W), and elucidate how H_2-induced swelling influences both the elastic and failure behavior of Mt. Furthermore, we provide molecular-level insights into the mechanisms by which H_2 modulates swelling and alters the

4

mechanical properties of Mt. To the best of the authors' knowledge, this is the first study to quantitatively evaluate, in a consecutive and integrated manner, the swelling behavior and mechanical property changes associated with H_2 storage in Mt from a molecular perspective.

Methodology

System Preparation

Montmorillonite (Mt), a well-studied member of the smectite clay mineral group, was selected as a representative layered silicate for this study. Its high sensitivity to water,[18] low mechanical strength,[19] and prevalence in reservoir caprock[20] have made it a focal point in the evaluation of geological gas storage. Mt is particularly relevant due to its association with the development of the instability of clay-rich formations.[21] Structurally, Mt features a three-layer (TOT) arrangement composed of an octahedral sheet (O-sheet) sandwiched by two tetrahedral sheets (T-sheet).[22] The chemical composition of the sodium-saturated Mt is $Na_{0.75}[Si_{7.75}Al_{0.25}](Al_{3.5}Mg_{0.5})O_{20}(OH)_4$. Isomorphic substitutions were introduced in accordance with Loewenstein's rule, ensuring that no two substitutions occurred at adjacent sites. An extended unit cell (UC) slab was constructed and replicated 8×4 times in the x-(41.28 nm) and y-(35.86 nm) directions, respectively, to form a larger three-layer structure with varying interlayer spacings. As Mt in caprock varies with depth and can host different water saturation, and given our previous findings that H_2 can potentially penetrate sub-nanopores of Mt and occupy these confined spaces,[12] we modeled the H_2 gas phase under varying water saturation conditions. Accordingly, the H_2 content considered varied from 0 to 1.25 per UC (0 to 40 molecules per system), whereas the water content varied between 0 to 10 molecules per UC (0 to 320 molecules per system).

Molecular Dynamics Simulations

All MD simulations were performed using LAMMPS open-source software.[23] For modeling the clay mineral slab, the accurate and well-known force field CLAYFF[14] was used. This force field predominantly employs Lennard-Jones and Coulomb potentials to model non-bonded interactions within the clay slab, while bonded interactions are utilized to accurately simulate the hydroxyl structure. The interlayer water molecules were represented by the

SPC/E model[24] that is compatible with CLAYFF force field.[14] A two-site model developed by Yang *et al.*[25] was also applied to H_2 molecules, we previously confirmed its accuracy for modelling in clay systems.[7] Our simulation workflow consists of two main stages. First, we design the system to explore how H_2 induces crystalline swelling. Then, we investigate how this swelling affects the mechanical properties of the system.

Crystalline Swelling Process

Initially, each clay system containing different numbers of H_2 and water molecules underwent energy minimization, followed by NPT simulations at $T = 373\,\text{K}$ and $P = 10\,\text{MPa}$ for 2 ns and 20 ns with time steps of 0.01 fs and 1 fs, respectively, to reach a stable interlayer distance. The final configurations were obtained through an additional 5 ns NVT simulation prior to the evaluation of the mechanical properties. Energy minimization was carried out using the conjugate gradient method with convergence criteria of 10^{-6} kcal/mol for energy and 10^{-8} kcal/(mol·Å) for stress. In the NPT and NVT simulations, the damping parameters of the Nosé–Hoover thermostat and barostat were set to 100 and 1000 times the integration time step, respectively. Periodic boundary conditions were applied in all three directions. A cut-off radius of 13 Å was used for short-range nonbonded interactions, while long-range electrostatic interactions were computed using the Ewald summation method with an accuracy of 10^{-5}. The comparison of Mt swelling values with experimental data and previous MD simulation studies is provided in the Supporting Information (SI), Table S1, and details of the energy- and trajectory-based analyses used to evaluate the impact of H_2 on Mt swelling are also presented therein.

Mechanical Properties

The mechanical response of the Mt systems was quantified by analyzing their stress and elastic tensors. The stress tensor, σ_{ij}, is obtained from the virial expression:

$$\sigma_{ij} = -\frac{1}{V_0}\left[\sum_{i=1}^{N} m_i\left(\mathbf{v}_i\mathbf{v}_i^T\right) + \sum_{i<j}\mathbf{r}_{ij}\mathbf{f}_{ij}^T\right], \tag{1}$$

where i and j run over all particles $(1 \le i, j \le N)$. In this expression, m_i, $\mathbf{v}_i$, $\mathbf{r}_{ij}$, and $\mathbf{f}_{ij}$ denote the mass, velocity, displacement vector, and interatomic force acting on particle i due to particle j, respectively. To describe the elastic behavior, the fourth-rank elastic stiffness tensor C_{ijkl} is introduced. This tensor is defined as the second derivative of the potential energy u with respect to the strain components ε_{ij} and ε_{kl}, normalized by the reference cell volume V_0:[26]

$$C_{ijkl} = \frac{1}{V_0}\frac{\partial^2 u}{\partial\varepsilon_{ij}\,\partial\varepsilon_{kl}}, \quad i,j,k,l \in \{1,2,3\}. \tag{2}$$

Here, the indices i, j, k, and l correspond to Cartesian directions. The stress and strain tensors are related through Hooke's law, which for small deformations can be expressed as:

$$\sigma_{ij} = C_{ijkl}\,\varepsilon_{kl}, \quad i,j,k,l \in \{1,2,3\}. \tag{3}$$

Details of the stress tensor components are provided in Figure S1, SI. Although this tensorial form is rigorous, it is not practical for computational analysis. Therefore, Hooke's law is often reformulated in the Voigt notation, which replaces double indices (ij) by single indices (1 to 6). The mapping is given as $(11) \to 1$, $(22) \to 2$, $(33) \to 3$, (23) or $(32) \to 4$, (13) or $(31) \to 5$, and (12) or $(21) \to 6$.[27] With this convention, the fourth-rank stiffness tensor is reduced to a 6×6 matrix form. Due to the orthotropic symmetry of clay platelets, only nine independent stiffness coefficients are needed to characterize the nanoscale elastic response.[28] These coefficients can be grouped into two categories: in-plane (C_{11}, C_{22}, C_{12}, C_{66}) and out-of-plane (C_{13}, C_{23}, C_{33}, C_{44}, C_{55}). This distinction reflects the anisotropic nature of layered materials, where in-plane bonding differs significantly from interlayer interactions. Under the Voigt notation, Hooke's law becomes:

$$
\begin{bmatrix} \sigma_1 \\ \sigma_2 \\ \sigma_3 \\ \sigma_4 \\ \sigma_5 \\ \sigma_6 \end{bmatrix} = \begin{bmatrix} C_{11} & C_{12} & C_{13} & 0 & 0 & 0 \\ & C_{22} & C_{23} & 0 & 0 & 0 \\ & & C_{33} & 0 & 0 & 0 \\ & \text{sym} & & C_{44} & 0 & 0 \\ & & & & C_{55} & 0 \\ & & & & & C_{66} \end{bmatrix} \cdot \begin{bmatrix} \varepsilon_1 \\ \varepsilon_2 \\ \varepsilon_3 \\ \varepsilon_4 \\ \varepsilon_5 \\ \varepsilon_6 \end{bmatrix} \tag{4}
$$

where "sym" indicates symmetric terms that are not explicitly written. This compact form facilitates both computational evaluation and physical interpretation of the elastic properties of Mt. Further details on the conceptual definition of stiffness coefficients are provided in Table S2, SI.

Several methods exist to calculate the stiffness coefficients, including the stress-fluctuation,[29,30] strain-fluctuation,[31,32] and constant-strain methods.[33,34] In this study, the constant-strain method was employed due to its proven reliability.[35,36] In this method, the system is first energy-minimized and then systematically deformed along 12 independent strain directions. The strain in each direction varied from -0.01 (compression) to $+0.01$ (tension), with a step size of 10^{-4}. The reported stiffness coefficients correspond to the average tensile and compressive responses in each principal direction.

To further analyze the mechanical response of Mt under tension and compression along the x-, y-, and z-directions, a second set of simulations was performed under uniaxial strain loading. In this setup, the simulation box was stretched or compressed in one direction, while pressure and temperature were maintained in the other two directions. The temperature was fixed at $373\,\text{K}$ in all directions, with zero pressure in the x- and y-directions and $10\,\text{MPa}$ in the z-direction, regulated using the Nosé–Hoover thermostat (damping parameter: $100\,\text{fs}$) and barostat (damping parameter: $1000\,\text{fs}$). Pressure was controlled in the two unstrained directions, while the third was deformed at a prescribed strain rate of $10^{-7}\,\text{fs}^{-1}$, consistent with previous studies demonstrating insensitivity of the results to this value.[37–39]

The maximum applied strain reached 0.4. A detailed validation of the simulation frame-work—including comparisons with MD and experimental data—is provided in the SI, Table S1 for swelling behavior and Tables S3–S5 for mechanical behavior, confirming the accuracy and robustness of the employed methods. Note that a detailed description of all analyses adopted in this work is provided in the SI.

Results and Discussion

To investigate the swelling behavior and mechanical properties of Mt under varying water and H_2 contents, we focused on interlayer dynamics and structural responses. By analyzing basal spacing, hydration energy, intercalation mechanisms, and both elastic and failure behaviors, we elucidate how interlayer water and H_2 affect Mt's nanoscale interactions and macroscopic properties, offering insights relevant to geological and engineering applications.

Impact of H_2 on the Basal Spacing

Figure 1a illustrates the definition of the basal spacing, d_{001}, while its variation as a function of interlayer hydration and H_2 is shown in Figure 1b. In the absence of both water H_2, the d_{001} of anhydrous Mt is 9.7 Å. With the increase of interlayer water to 1.25 water molecules per unit cell (UC) (40 H_2O confined within 32 UCs, represented by red line in Figure 1b), this spacing increases to 11.5 Å due to formation of a monolayer (1W) hydration state. Further water uptake to 5 H_2O/UC slightly expands d_{001} to 12.6 Å, remaining in the stable 1W state. Above 5 H_2O/UC, the d_{001} expands sharply to approximately 14.0 Å, passing through a transition region with a steep slope in the d_{001} curve and reaching the next configuration, in which water molecules arrange into a double layer (2W) hydration state. This state remains stable up to approximately 10 H_2O/UC, with the d_{001} of $\sim$ 16 Å after which triple layer (3W) configuration takes over. The spacing in all states of Mt is consistent with values reported in the literature (see Table S1).[40,41]

Under anhydrous conditions, upon exposure to H_2, the Mt interlayer expands to accommodate gas molecules by modifying the balance of intermolecular forces[42] and enhancing interlayer repulsion (Figure 1b, red line). In the presence of water (Figure 1b, pink to grey lines), the impact of H_2 on the interlayer spacing is minimal during stable 1W regions, yet it is prevalent during the transition between these hydration states. This behavior can be described as an 'expansion–filling–saturation" process.[42,43] Therefore, H_2 primarily affects

anhydrous conditions and transition regions, accelerating the onset of interlayer expansion to the next stable hydration state. For instance, the 1W→2W transition without H_2 occurs when interlayer hydration reaches ~ 5 H_2O/UC (160 water molecules), yet with H_2 this transition occurs as early as 3.75 H_2O/UC (120 water molecules). This effect scales with H_2 content, with 20 H_2 molecules showing intermediate behavior. In the 2W $\rightarrow$ 3W transition, H_2 further increases the interlayer spacing and accelerates the transition, with a cumulative impact on swelling. Interestingly, unlike the 1W stable region—where the presence of H_2 had minimal structural impact—the 2W stable region exhibits a more pronounced difference in d_{001} depending on the H_2 content.
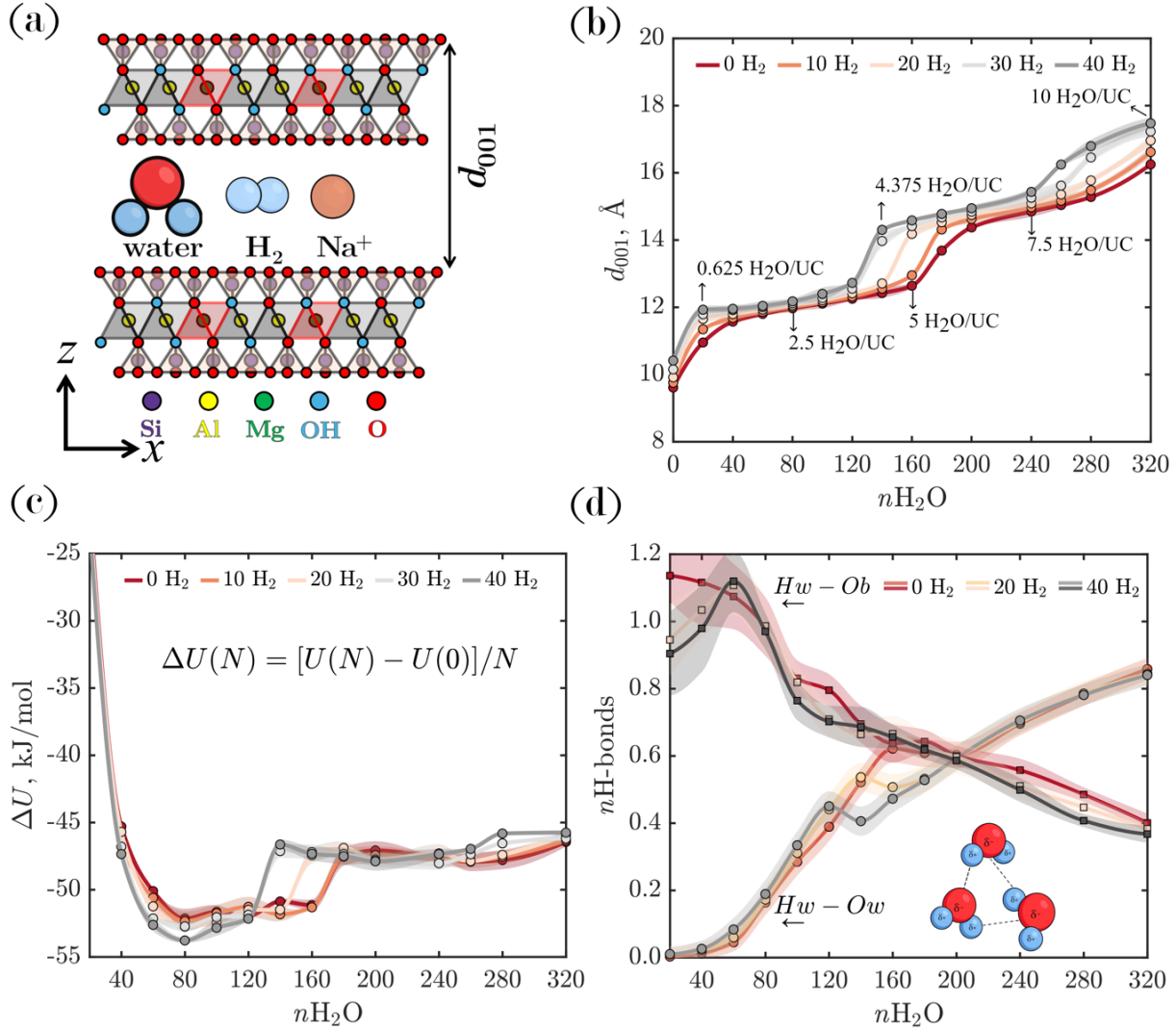
Figure 1: (a) Schematic of the system containing water, H_2, and cations, with basal spacing, d_{001}, defined as the distance from the top of one clay layer to the top of the next. (b–d) Variation of key structural and energetic properties of montmorillonite (Mt) as a function of water content (0 to 320 per 32 UCs) under different H_2 loadings (0 to 40 H_2 molecules per system): (b) d_{001}; (c) average hydration energy ($\Delta U(N)$); (d) average number of H-bonds per water molecule, including water–surface oxygen of Mt (Hw–Ob) and water–water (Hw–Ow). For clarity, panel (d) includes results for systems with 0, 20, and 40 H_2 molecules only. The shaded region denotes the mean value $\pm$ standard deviation calculated over the equilibrium time window.

Figure 1c shows the changes in average hydration energy, $\Delta U(N)$, with increasing H_2 content. During the 1W stage, $\Delta U(N)$ of Mt decreases rapidly and eventually falls below the internal energy of pure SPC/E water model, which is around -41.5 kJ/mol,[44] indicating

that the system would readily rehydrate if water were available. While all systems initially follow a similar trend, the presence of H_2 leads to a greater reduction in $\Delta U(N)$, resulting in an even deeper global energy minimum. In the case of Mt (Figure 1c, red line) without H_2, the minimum energy region is relatively broad (spanning from 1.85 to 5 H_2O/UC), indicating energetic favorability across a wide range of hydration. In contrast, while the systems containing H_2 exhibit lower overall potential energy, the well is much narrower (between 1.85 and 3.75 H_2O/UC), implying that their stability is energetically favorable only within a limited hydration range. In other words, H_2 facilitates a lower-energy pathway for enhanced swelling. This suggests that H_2-containing systems may exhibit reduced structural resilience when exposed to fluctuations in water content.

Interlayer Molecular Interactions Driving Swelling

To understand the molecular interactions responsible for the observed swelling behavior, we examine how H_2 molecules influence the behavior of other species (cations and water) within the Mt interlayer. Figure 2 shows linear atomic density profiles across the simulation box, perpendicular to the clay layer (along z-axis).

In anhydrous Mt, charge-balancing Na^+ ions form inner-sphere surface complexes (ISSCs), directly coordinated to the clay surfaces (Figure 2, yellow line, showing two distinct peaks at ~ 9 Å from the peaks corresponding to surface oxygen, O_b). Formation of ISSCs at distances less than 1.16 Å, the ionic radius of the cation, indicates considerably closer coordination over the surface's hexagonal cavities.[45,46] In contrast, when H_2 is absent, with increased hydration, Na^+ ion becomes hydrated and moves toward the interlayer center, positioning at 3.1 Å from the surface as an outer-sphere surface complex (OSSC). At low hydration levels, this occurs for only a few Na^+, while others remain near the surface, determined by the available water to fully hydrate each cation.[40] This progression underscores the central role of Na^+ hydration energy in driving the swelling behavior of the clay.[47] Presence of H_2 at very low water content (0.625 H_2O/UC) shifts Na^+ slightly toward the clay slabs. However,

as hydration increases, Na^+ is gradually moved into the OSSC. More intensely, under 2W hydration (*e.g.*, 7.5 H_2O/UC), when a large amount of H_2 is present (*e.g.*, 40 H_2), it positions itself between the clay surface and the cation, weakening the electrostatic interaction and allowing some Na^+ ions to drift into the geometric center of the interlayer space. This observation is further supported by the radial distribution function (RDF) between Na^+ and surface oxygen atoms ($Na–O_b$), which indicates a shift toward configurations characteristic of increased hydration (Figure S3, SI). Therefore, from the viewpoint of cation hydration, H_2 facilitates the relocation of Na^+ into a hydrated state before the formation of a stable 1W layer. Once the 1W structure is established, however, H_2 has little influence on the arrangement of the interlayer components. In the 2W state, H_2 tends to shift Na^+ ions toward the center of the interlayer, indicating a greater contribution of cation hydration to the observed swelling.
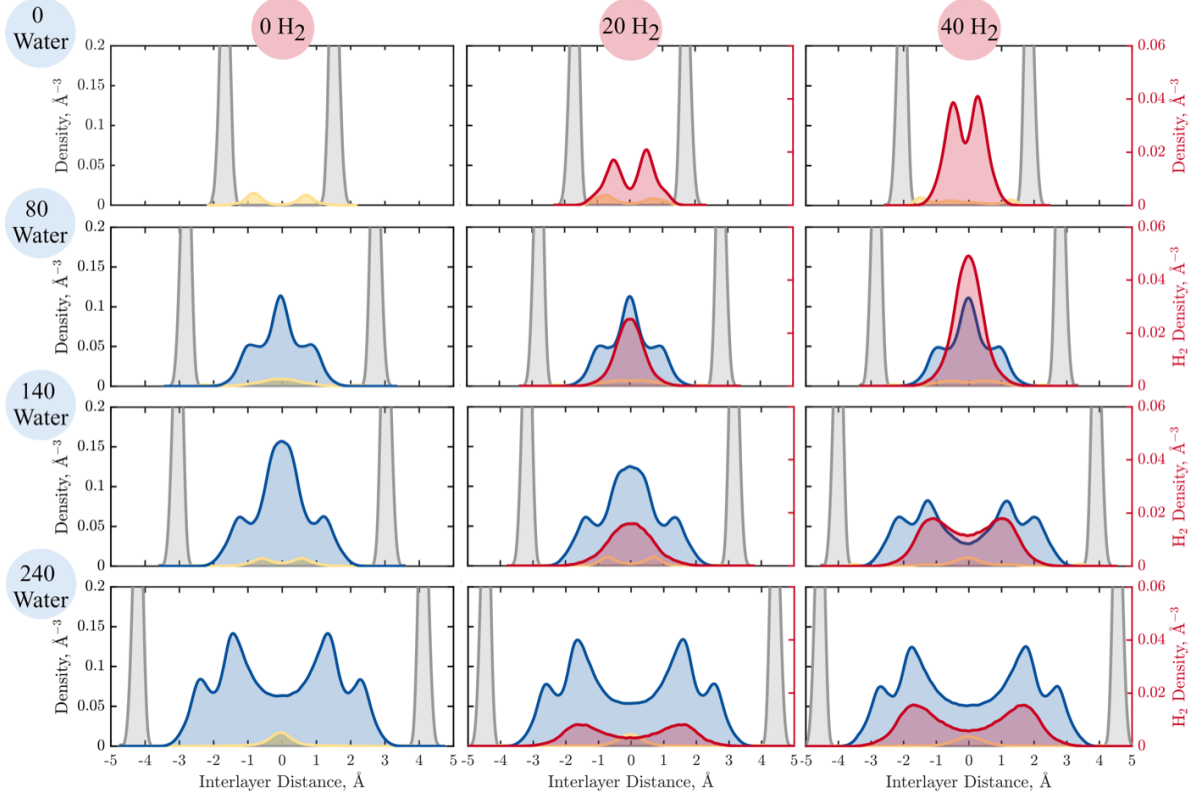
Figure 2: Atomic density profiles of H_2O (blue), H_2 (red), Na^+ (yellow), and Ob atoms of the clay surface (gray) at four different water contents representing dry clay (0 water; 0 H_2O/UC), a single water hydration layer (80 water; 2.5 H_2O/UC), a transition region (140 water; 4.375 H_2O/UC), and two water hydration layers (240 water; 7.5 H_2O/UC). Each profile is shown for three different H_2 contents, highlighting the spatial distribution of species relative to the clay surface under varying hydration and H_2 conditions.

An important interaction mechanism arises from the steric effects of H_2, together with its gas-like behavior (not dissolved in water) and preferential distribution (Figure 3a), which tend to compress water molecules more closely together (see Figure S4, SI). This spatial confinement promotes H-bond formation among water molecules, thereby accelerating the organization of the water molecular structure. As shown in Figure 1d, H_2 enhances the water network by increasing H-bonding between water molecules (Hw-Ow), particularly at low water content. However, the transition to the 2W hydration state disrupts this network, as the formation of a second hydration layer, driven by the overall volume increase—allows water molecules to move further apart. These results also indicate that, in the 2W system, the presence of H_2 has a negligible effect on Hw-Ow H-bonding. Note that as expected,

16

Hw-Ow H-bonds in nanopores are significantly lower than in bulk ($\sim$ 3.5 H-bonds per water molecule in bulk). In addition, increasing water generally reduces water–Mt H-bonds.

Indeed, the low solubility of H_2 in water impacts its spatial distribution, particularly when its concentration exceeds the solubility limit (0.08 mol/kg, which is 1.44 $\times 10^{-3}$ H_2 per 1 H_2O).[48–50] Figure 3b,c present side and top views of the 2D density distribution of H_2 under different hydration states. At water content below 1W hydration state, H_2 appears to be uniformly distributed along the clay surface. As the water content increases and the system transitions toward a 1W and 2W hydration state (Figure 3b, system 80 water (2.5 H_2O/UC) and 140 water (4.375 H_2O/UC)), H_2 begins to aggregate into gaseous domains, forming distinct feature of plumes. A closer examination of the side view reveals that, in the 1W state, these H_2-rich clusters are confined by surrounding water molecules, which limits their lateral mobility within the xy-plane. Similarly in the 2W system, although this confinement is relaxed and H_2 localize within each hydration layer, they are still connected as a single cohesive plume without any interruption from water molecules (Figure 3c, system 240 water (7.5 H_2O/UC), 20 and 40 H_2). It should be noted that H_2 nano-bubbles in bulk tend to form circular, symmetric shapes because this geometry minimizes the surface area for a given volume, thereby reducing surface energy according to the Laplace pressure principle.[51] In contrast, our findings show that under Mt nano-confined environments with interlayer distances below 2 nm, H_2 molecules form asymmetric bubble morphologies. These morphologies largely driven by the locations of isomorphic substitutions in the Mt's octahedral sheet, O-sheet, (Figure 3c shown over the water 2D density map by light green), where the arising negative charge due to Mg^{2+} substitution for Al^{3+} defines the local water–cation arrangement, thereby influencing the shape of the gas domain.
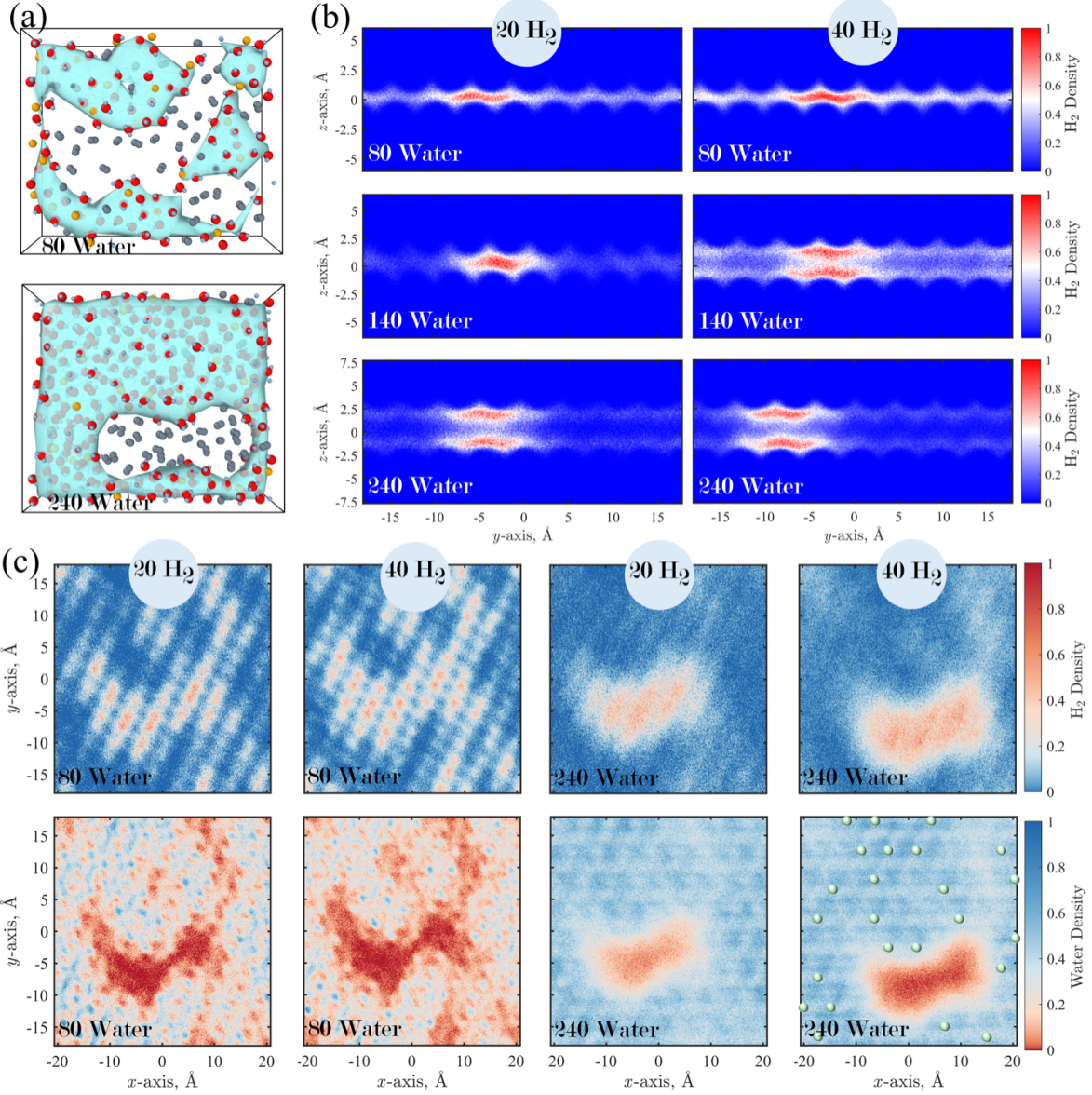
Figure 3: (a) 3D visualization of confined fluid between two Mt slabs (not shown, positioned above and below the presented layer) over the xy-plane, comparing systems with one (80 water, 2.5 H_2O/UC) and two (240 water, 7.5 H_2O/UC) hydration layers. H_2 is shown as gray van der Waals (vdW) spheres, water oxygen atoms are red, hydrogen atoms are white, and the water surface is rendered in transparent cyan. (b) 2D density maps of H_2 projected onto the yz-plane for different water and H_2 contents, showing H_2 plume formation. (c) 2D density maps in the xy-plane of H_2 (top row) and water (bottom row) for the different systems, illustrating the spatial distributions of the components at varying water and H_2 contents.

Furthermore, we investigated the orientation distribution of water molecules near the clay surface (Figure 4a) and the corresponding average orientation population profiles (Figure 4b).

18

In the absence of H_2 and within the 1W hydration layer, water molecules exhibit strong orientational ordering near the clay surface, characterized by a distribution range of 110° to 160° and distinct average angular peaks centered around 135° (and 45° on the opposing surface). These orientations correspond to water molecules approaching the surface with one of their hydrogen atoms pointing toward it. As the system approaches the transition region and the formation of the 2W hydration layer, water molecules become increasingly aligned with the surface normal, with the orientation angle range progressively shifting toward $\sim 130°$ to $\sim 170°$. This indicates configurations in which both hydrogen atoms face the clay slab. Overall, this trend suggests stronger dipole alignment of water molecules toward the clay surface as hydration increases (Figure 4c).

The introduction of H_2 molecules has no tangible impact on the orientation of water near the surface when stable 1W and 2W hydration layers are formed. In contrast, as shown in Figure 4b, increasing the number of H_2 molecules gradually shifts the average orientation angle of water molecules near the surface in the transition region (140 water molecules in the system), with the average peak moving from $\sim 140°$ to $\sim 150°$. This shift indicates that the occupation of the interlayer midplane by H_2 molecules pushes water molecules closer together, as explained earlier, forcing them to adopt configurations in which both hydrogen atoms are oriented toward the clay surface.
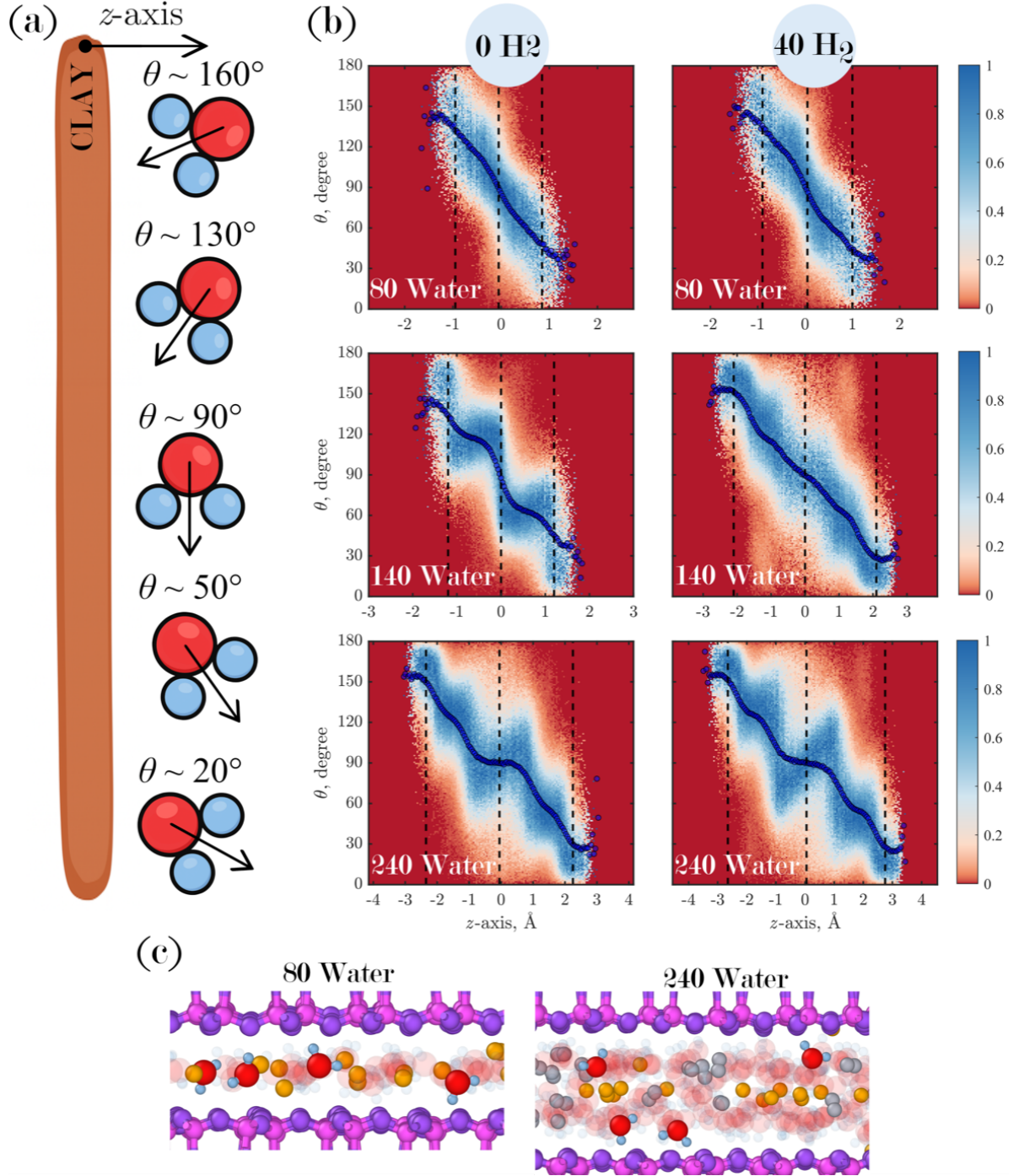
Figure 4: (a) Schematic diagram of water orientation, defined as the angle between the water dipole moment and the z-direction (normal to the clay slab, shown in brown), (b) population of the angle formed in the interlayer along the z-direction, from one top of the clay slab to the other. The two dashed lines on either side indicate the peaks of the water number density in the interlayer, and the blue line represents the average orientation population, and (c) illustration of water orientation in two different systems: 80 water molecules (2.5 H_2O/UC) without H_2, and 240 water molecules (7.5 H_2O/UC) with 40 H_2 molecules.

In summary, H_2 accelerates the formation of stable water layers in both 1W and 2W configurations at lower water contents, promoting clay swelling during anhydrous conditions and hydration state transitions (Figure 1b). This deepens the hydration energy minimum but narrows the stable hydration range, indicating reduced structural resilience (Figure 1c). Indeed, H_2 repositions Na^+ ions, weakening clay–cation interactions in anhydrous clay and enhancing hydration in the 2W state (Figure 2). The steric effects of H_2 promote H-bonding at low water content but has little effect in 2W systems (Figure 1d), while higher water content promotes water localization within the interlayer rather than at the Mt surface.

In these nano-confinements, H_2 forms asymmetric gas plumes, influenced by O-sheet clay substitutions (Figure 3). H_2 disrupts water orientation in the transition region without a considerable impact on the 1W and 2W states (Figure 4). It should be noted that T-sheet substitutions are relatively uncommon in Mt. In contrast, O-sheet substitutions impose a weaker electrostatic influence on interlayer ions. As a result, the spatial distribution of interlayer Na^+ is more strongly dictated by T-sheet substitutions, which can in turn enhance the development of plume-like ion arrangements.

Elastic Response under Hydration and H_2

Figure 5 shows all elastic stiffness coefficients of Na-Mt with variable interlayer water and H_2 content, reflecting the anisotropic mechanical behavior arising from the stiff clay basal planes and the mechanically soft interlayer. The in-plane coefficients (C_{11}, C_{22}, C_{12}, and C_{66}) (Figure 5a-c) describe deformation within the Mt crystal structure, while the out-of-plane coefficients (C_{13}, C_{23}, C_{33}, C_{44}, and C_{55}) (Figure 5d-h) characterize the mechanical response involving the interlayer space.

As expected from the layered silicate structure, the in-plane coefficients are significantly higher than the out-of-plane coefficients, with the C_{11}/C_{55} ratio of around 45 for the dry system, underscoring the strong intralayer covalent/ionic bonding and the relatively weak van der Waals and H-bonding in the interlayer. This pronounced anisotropy is consistent with findings from previous molecular simulations and experimental studies.[34,52,53] Among the in-plane coefficients, C_{11} is the highest, followed by C_{22}, C_{12}, and C_{66}, the last of which reflects shear stiffness within the basal plane and is the lowest among the group. This is consistent with trends reported in both experimental and first-principles investigations.[54,55] Notably, C_{11} and C_{22} differ by $\sim 6\%$, which falls within the range (2–10%) reported for other phyllosilicates.[56,57]

Increasing interlayer water content reduces all in-plane coefficients, regardless of the amount of H_2 present, particularly pronounced at low hydration levels. For example, adding 20 water molecules to the dry system decreases in-plane coefficients by $\sim 12\%$ on average. In contrast, H_2 alone leads to smaller reductions from 1.5 to 9% for 20 to 40 H_2 molecule systems, with the magnitude of this effect varying depending on the hydration level. This trend has been attributed to an increase in basal spacing and has been previously reported for CO_2-containing clay swelling systems.[58,59]

In contrast, the out-of-plane coefficients show greater sensitivity to shear and normal stresses perpendicular to the layers than to basal spacing, and drop significantly with the addition of initial water or H_2. For example, the addition of 20 water molecules reduces

out-of-plane coefficients by 50 to 75%. The entry of the first water and H_2 molecules into the interlayer space of the dry system results in a much greater reduction in out-of-plane coefficients than in in-plane ones. Interestingly, at higher hydration levels (60 water molecules in the system, 1.875 H_2O/UC), a partial recovery of certain out-of-plane coefficients is sometimes observed. This non-monotonic behavior has previously been attributed to the formation of structured water networks and an average increase in H-bonding between Mt and water (see Figure 1d).[59] As the number of water molecules increases beyond 60, the out-of-plane coefficients tend to fluctuate around a steady value, without showing a specific trend or dependence on the H_2 concentration, but exhibiting heightened fluctuations at higher H_2 levels. This triphasic behavior, initial softening, partial stiffening, and subsequent oscillatory response, has been described as a characteristic feature of water-induced mechanical transitions in swelling clays and remains applicable to the H_2-containing system.[28,60]
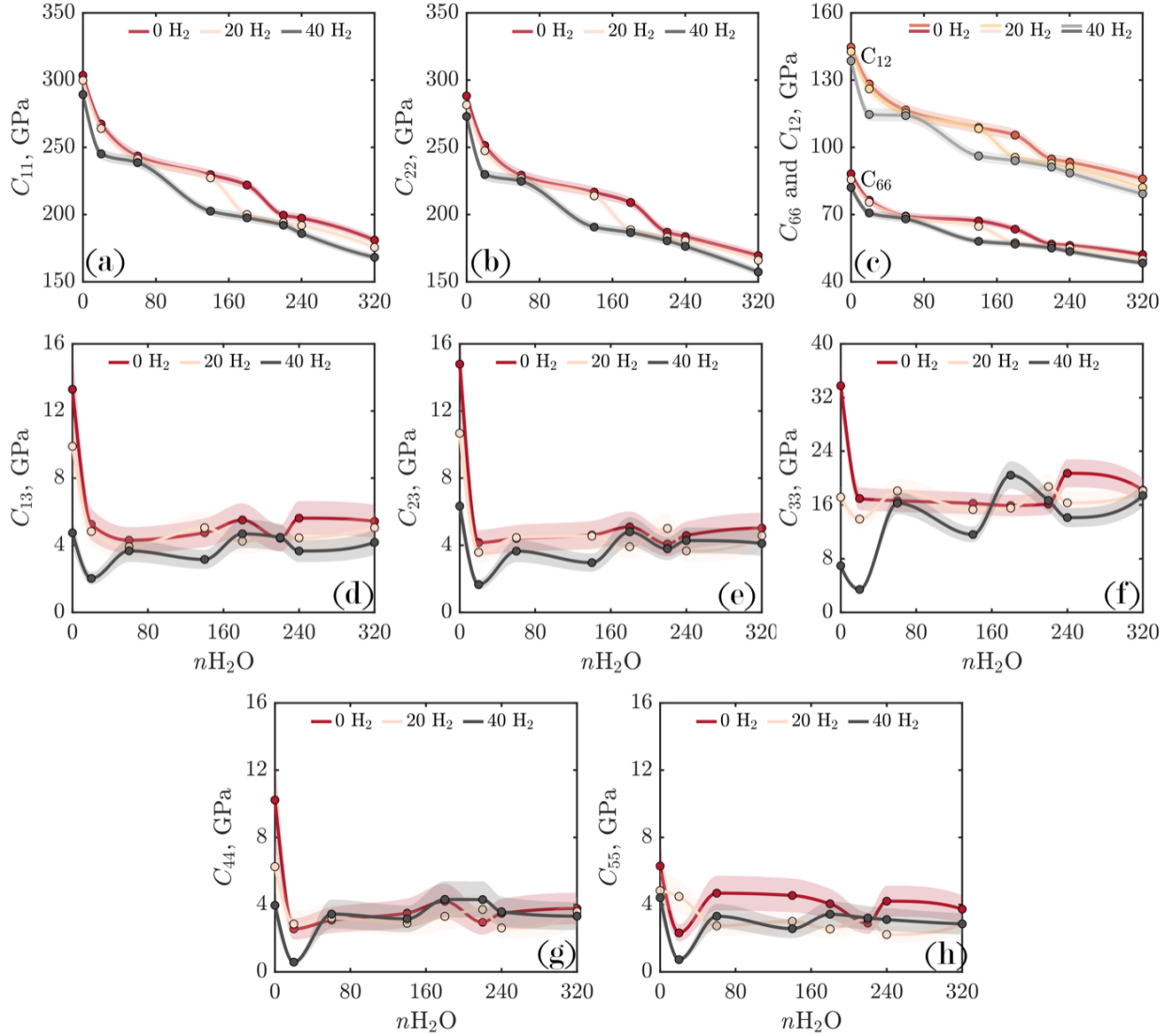
Figure 5: Directional elastic stiffness coefficients of Mt as a function of interlayer water contents (0, 20, 60, 140, 180, 220, 240, and 320 molecules) and H_2 contents (0, 20, and 40 molecules): (a–c) in-plane stiffness coefficients (C_{11}, C_{22}, C_{12}, and C_{66}); (d–h) out-of-plane stiffness coefficients (C_{13}, C_{23}, C_{33}, C_{44}, and C_{55}). The shaded area indicates the mean value $\pm$ standard deviation from repeated simulations.

Furthermore, the bulk modulus (K, resistance to volumetric change), shear modulus (G, resistance to shape change), and Poisson's ratio (ν, ratio of lateral to axial strain) of Mt systems as a function of interlayer water and H_2 content are presented in Figure S5, SI. The variations in K and G as a function of water and H_2 content reflect a combination of the stiffness trends of in-plane and out-of-plane coefficients, described above. Overall, increasing

24

water and H_2 content leads to a decrease in both K and G, although some exceptions occur due to the stiffness contribution of out-of-plane coefficients. This decrease is most pronounced when moving from the dry system to systems with low water and H_2 content. In contrast, ν does not follow a systematic trend with water or H_2 content, but instead shows irregular fluctuations.

Effect of Induced Swelling on Elastic Behavior

Water and H_2 have a paradoxical influence on the in-plane stiffness coefficients, exhibiting both reinforcing and weakening effects. Given the positions of Si and Al in tetrahedral and octahedral sites, respectively, analyzing interactions between them and surrounding oxygens can reveal key factors on the structural stability of Mt. Figure S6, SI, illustrates the RDFs of Al$\cdots$O and Si$\cdots$O bonded pairs at varying levels of water and H_2 content. Across different systems, the positions of the first peaks remain unchanged (1.93 Å for Al$\cdots$Ob, 1.93 Å for Al$\cdots$Oh, and 1.58 Å for Si$\cdots$Ob). However, increasing the water and H_2 content amplifies the first peak in all three cases, indicating strengthened interactions in these bonded pairs.[37,61] As a result, higher water and H_2 content marginally enhance the strength of the intralayer clay structure. These changes in intralayer interactions may be related to variations in the attractive and repulsive forces between the Mt layers and the interlayer, resulting from changes in interlayer content.[42] Despite this local strengthening, as discussed earlier, the in-plane coefficients decrease as interlayer water and H_2 content increase, expanding the interlayer distance and enlarging the cross-sectional area (A) over which the force (F) is distributed. This geometric effect (*i.e.*, the impact of induced swelling) lowers the stress ($\sigma = F/A$) for a given force. Consequently, the in-plane coefficient, proportional to the stress–strain ratio, decreases with increasing basal spacing. This geometrically induced softening outweighs local structural reinforcement, making the coefficients depend more on basal spacing than on bond strength, highlighting the interplay between structural and geometric factors in hydrated Mt elasticity.

The geometric mechanism associated with variations in basal spacing does not affect the out-of-plane coefficients, since cross-sectional area A for shear or normal (z-direction) forces remains constant. However, water weakens these coefficients by replacing strong Na^+–Mt electrostatic interactions with weaker H-bonds and by forming hydration shells that displace Na^+ from the Mt surface (Figure 2). In contrast, non-polar H_2 does not form H-bonds with the Mt surface nor hydrate Na^+ ions; instead, it disrupts ionic bridges without forming compensatory bonds. In the absence of interlayer water or H_2, Na^+ ions become locked between the Mt layers, often located next to isomorphic substitutions. However, in the presence of H_2, the high mobility of the gas molecules alters the positions of Na^+ ions. The initial incorporation of either water or H_2 acts as a lubricant, reducing interlayer friction and promoting slippage between Mt layers, which in turn, lowers the system's shear strength. Importantly, this molecular inclusion significantly weakens Na^+–Mt interactions, with the binding interaction energy dropping from -12769 ± 10 kJ/mol in the dry system to -9574 ± 14 kJ/mol (25%) and -10605 ± 11 kJ/mol (17%) following the addition of 20 water molecules and 20 H_2 molecules, respectively. This sharp reduction at the early stage highlights the extreme sensitivity of interlayer cohesion to even minimal amounts of water or H_2.

Mechanical Failure Response under Hydration and H_2

The ultimate tensile strength (UTS) and ultimate compressive strength (UCS) are the maximum stresses a material can withstand under tension and compression, respectively, before failure. Accordingly, Figures S7 and S8, SI, were used to determine the UTS, UCS, and ultimate tensile and compressive strain values. Figure 6a-c presents the triaxial UTS and UCS values for Mt systems containing varying amounts of water and H_2. Pronounced mechanical anisotropy is evident: for every system studied, the UTS follows the order: $UTS_x > UTS_y > UTS_z$, whereas the UCS follows: $UCS_z > UCS_y > UCS_x$. These rankings, well documented in prior work—reflect the layered structure of Mt.[37,38,62] While two systems, 20 H_2O–20 H_2 and 60 H_2O–20 H_2, deviate slightly from the expected tensile-strength

ordering, the differences fall within the numerical uncertainty of the simulations; nonetheless, they illustrate that H_2 can locally perturb the anisotropy hierarchy. In all cases, the UCS exceeds the corresponding UTS, indicating a greater tensile vulnerability of clay, particularly along the z-direction, where plasticity precedes fracture. This observation is consistent with the macroscopic experimental findings of Zhang $et\ al.$[63,64] The dry system without H_2 shows the highest UTS in the z-direction, while the initial addition of 20 H_2 and 20 H_2O reduces UTS by 46% and 52%, respectively, due to disruption of Na^+–Mt ionic bonds, consistent with the out-of-plane stiffness coefficients (Figure 6c).
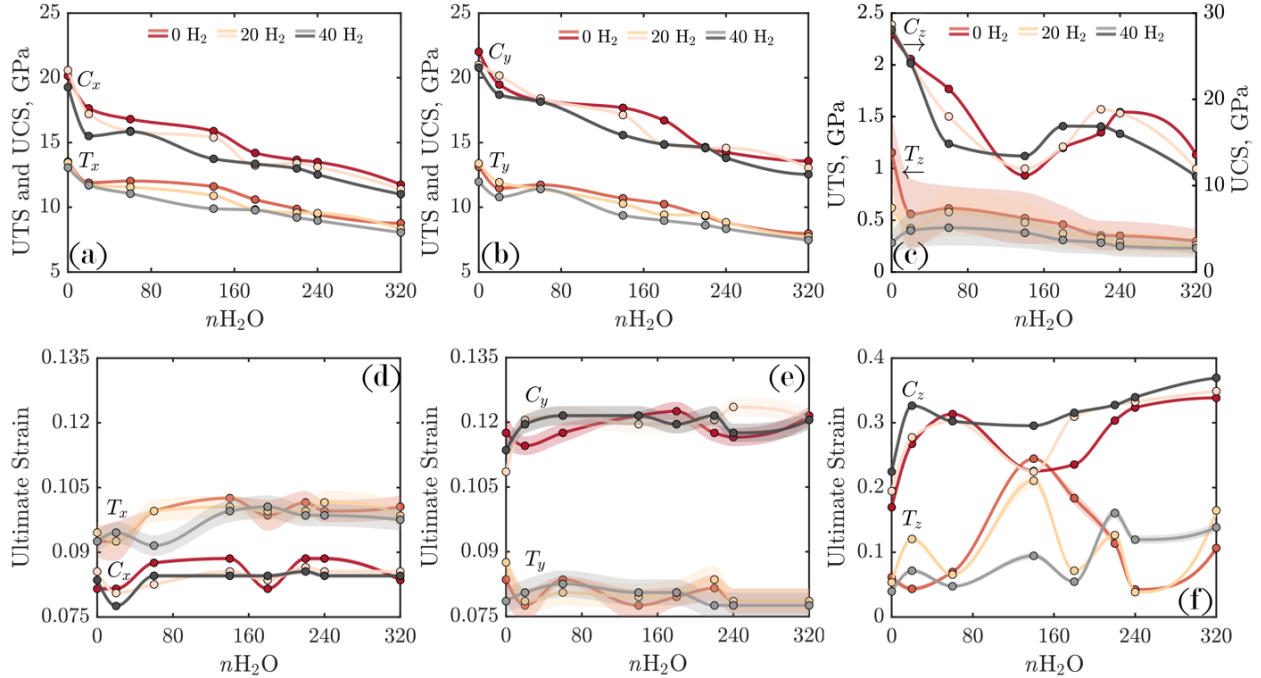

Figure 6: UTS and UCS (a–c) and ultimate strain (d–f) as a functions of interlayer water contents (0, 20, 60, 140, 180, 220, 240, and 320 molecules) and H_2 contents (0, 20, and 40 molecules) for systems loaded along the (a,d) x-, (b,e) y-, and (c,f) z-directions. The shaded area indicates the mean value ± standard deviation from repeated simulations.

The ultimate tensile strain and ultimate compressive strain ($i.e.,$ the strains at UTS and UCS) quantify the deformation a system can sustain before failure. As shown in Figure 6d-f, Mt slabs loaded in the x-direction tolerate, on average, 18% higher ultimate tensile strain than those loaded in the y-direction. Under compression, y-direction loading exhibits around

40% higher ultimate compressive strain than x-direction loading, reflecting greater ductility along y. Strain fluctuations are largest along the z-direction, consistent with the pronounced plastic response observed there (Figure 6c). Tensile loading in the y-direction initiates cracks faster than compression, whereas in the x-direction, compression causes earlier failure than tension. In addition, neither H_2 nor water significantly alters the ultimate strain in the x- and y-directions, and no consistent trend is observed across varying conditions (Figure 6d,e). In contrast, the z-direction shows non-monotonic variations: compressive ductility first increases, then decreases, and increases again with changing water content (Figure 6f). Our findings align with those of Zhao *et al.*[65] The dry, H_2-free system fails fastest in z-direction compression, while the most dramatic changes in ductility occur upon the first inclusion of guest molecules: introducing 20 water molecules or 20 H_2 molecules enhances z-direction ultimate compressive strain by 64% and 16%, respectively, relative to the dry reference. This arises from the much higher compressibility of systems containing water and H_2 compared to the dry, H_2-free system.

Mechanical Failure Behavior

Because the clay layers lie in the xy-plane, the in-plane *UTS* and *UCS* are governed by bond rupture within the Mt lattice and are determined from the elastic portions of the stress–strain curves for loading along the x- and y-directions, which exhibit constant slopes (Figures S7 and S8, SI). Given this linearity, *UTS* and *UCS* primarily depend on the corresponding elastic stiffness coefficients (C_{11}, C_{22}) and the ultimate tensile or compressive strain (Figure 6d,e). Consequently, the in-plane strength trends in Figure 6a,b reflect variations in C_{11} and C_{22} (Figure 5a,b) with minor deviations arising from differences in ultimate strains (Figure 6d,e). It should be noted that, as these coefficients vary systematically with basal spacing, in-plane *UTS* and *UCS* are likewise governed by this relationship, with ultimate strain playing a secondary role.

To further assess the role of atomic pairs in the *UTS* and *UCS* of the xy-plane, we examine

the structural deformation and the normalized number of broken bonds in the O- and T-sheets, focusing on Al–basal oxygen pairs (Al$\cdots$Ob), Al–hydroxyl oxygen pairs within the O-sheet (Al$\cdots$Oh), and Si–basal oxygen pairs within the T-sheet (Si$\cdots$Ob) under tension in the x- and y- directions. Figure 7 shows the visual analysis of mechanical asymmetry alongside the normalized stress distribution within the Mt structure for a selected system with 140 water molecules (4.375 H_2O/UC) and 40 H_2 molecules. Note that the virtual broken bond criteria follow Yang $et\ al.$,[66] using RDF cutoff radii of 1.84 Å for Si$\cdots$Ob, 2.66 Å for Al$\cdots$Ob, and 2.84 Å for Al$\cdots$Oh, consistent with established literature values[37,61] (see Figure S6, SI).

Considering the critical strain points A–D (Figure 7b,d), stage A corresponds to maximum stress (0.099 and 0.081 for the x- and y-directions, respectively, Figure 7a,c), marking failure. Stage B (0.107 in x- and 0.088 in y-directions) represents the post-failure phase, characterized by stress relaxation. With increasing strain, interlayer spacing decreases due to the Poisson effect. As shown by the renderings in Figure 7b,d, stress buildup is greater in the T-sheet than the O-sheet; however, normalized data reveal more bond fractures in the O-sheet despite its higher rupture threshold relative to the T-sheet. Under x-direction tension, bond breakage follows Al$\cdots$Ob $>$ Al$\cdots$Oh $>$ Si$\cdots$Ob, while in the y-direction it is Al$\cdots$Oh $>$ Al$\cdots$Ob $>$ Si$\cdots$Ob. Fractures initiate mainly in O-sheet bonds under x-direction tension before propagating to the T-sheet, indicating stronger tetrahedral bonding. Overall, Al$\cdots$Ob and Al$\cdots$Oh breaks are more frequent in y-direction tension, while Si$\cdots$Ob dominates under x-direction tension. These trends reflect not only bond strength but also bond orientation, atomic configuration, and mobility: Si$\cdots$Ob bonds in the T-sheet have tetrahedral coordination, whereas Al$\cdots$Ob bonds in the O-sheet are octahedral. Larger T-sheet displacements in x-direction tension yield higher fracture rates, consistent with the increased UTS along this axis. As shown in Figure 7b,d, stage A exhibits pronounced stress concentrations in the T-sheet. Following the fracture in stage B, stress localizes around crack sites within the T-sheet, where interlayer molecules apply additional pressure that promotes

crack growth. Most bond breakage occurs between stages A and B, after which the system stabilizes. Under x-direction tension, cracks are vertically aligned, in contrast to the more irregular patterns observed under y-direction tension. Note that the Si$\cdots$Ob broken bond diagram aligns closely with the stress–strain curve shown in Figure 7a,c (dashed line, right axis). No T-sheet bond breakage occurs during the linear stress increase, but the broken bond coincides exactly with the sudden stress drop, highlighting the T-sheet's critical role, over the O-sheet, in tensile failure. The variations in, and contributions of, each sheet to the system's total potential energy, shown in Figure S9, SI, further support this.

Bond breakage in the T-sheet enables interlayer molecules to penetrate the Mt structure (circle in stage A). Water infiltrates fractures more readily than H_2 due to stronger clay interactions (in the areas enclosed by black circles in stages B). With continued deformation, H_2 also enters alongside water, aided by its smaller size and higher diffusivity (circles in stage C). This co-penetration weakens interlayer bonds, reduces stress, and separates clay platelets. Under y-direction tension, platelets tilt and disconnect nanopores, while x-direction tension preserves or strengthens connectivity. At maximum x-strain (0.4, stage D), cracks widen to uptake water, and H_2 circulates through central channels—behavior absent under y-direction tension, where H_2 remains confined.
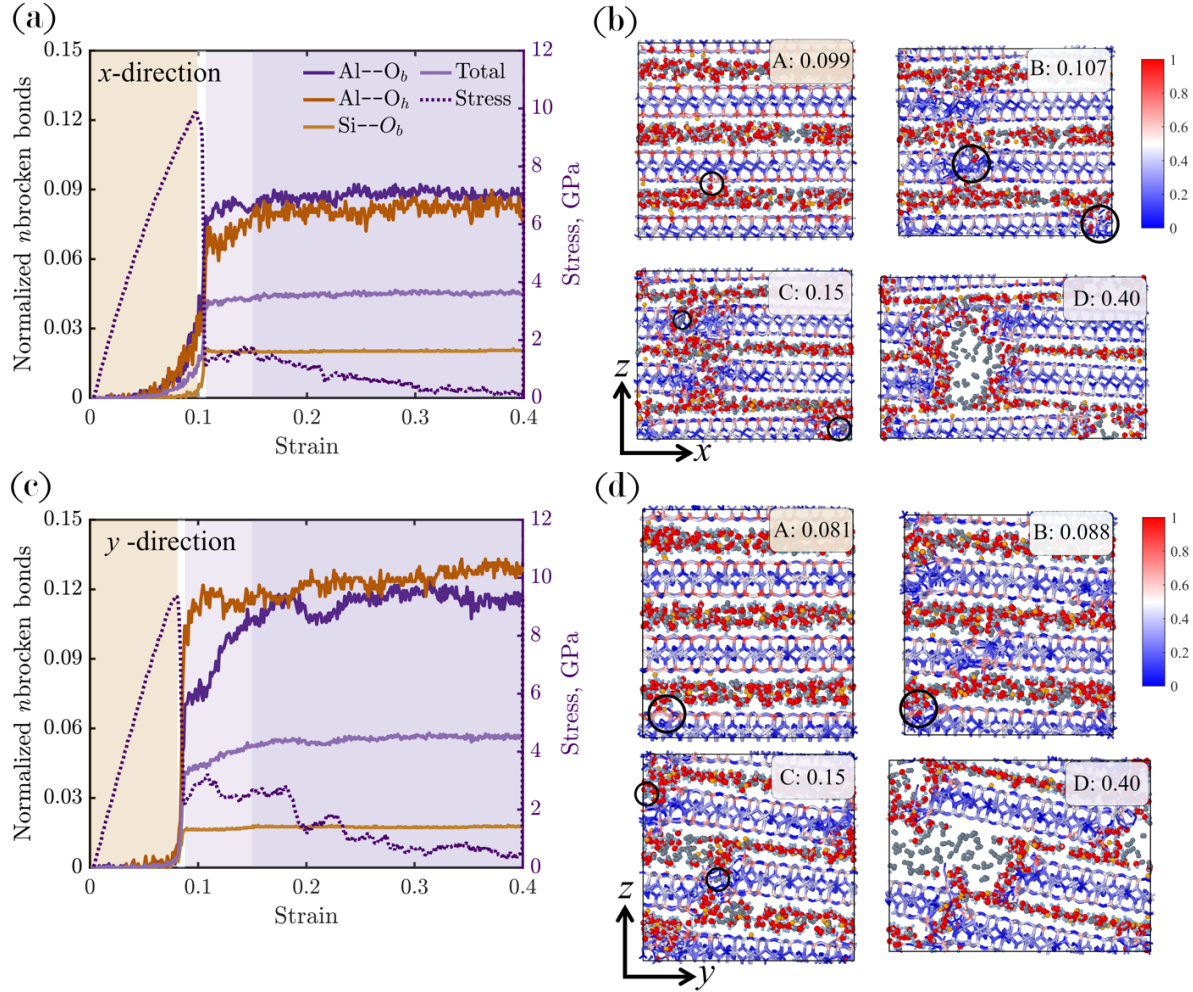
Figure 7: Normalized number of broken bonds for Al$\cdots$Ob and Al$\cdots$Oh in the O-sheet, and Si$\cdots$Ob in the T-sheet (left axis), together with the corresponding stress variation (right axis) at different strain levels for (a) x-direction and (c) y-direction tension in the system containing 140 water and 40 H_2 molecules. Panels (b) and (d) present visualizations and normalized stress distribution in the Mt structure during tensile loading at critical strain values in the (b) x-direction and (d) y-direction. According to the colormap, red and blue in the Mt structure indicate high and low stress values, respectively.

31

As shown in Figure 6c, increasing water and H_2 contents reduce the *UTS* in the out-of-plane direction. At higher water contents, the effect of H_2 becomes negligible and falls within the uncertainty range for 2W systems. Due to the surface charge of Mt, water–Mt H-bonds (Hw–Ob) are stronger than water–water bonds (Hw–Ow),[67] allowing Hw–Ob bonds to better resist separation under out-of-plane loading. To capture these effects in hydrated systems, we analyze the normalized number of broken Ob–Hw bonds. Figure 8a shows this metric for systems with 60 (1.875 H_2O/UC) and 240 (7.5 H_2O/UC) water molecules, with and without 40 H_2, from O (no strain) to D (final strain), along with the stress–strain curve (top right) for the 60-water system. O marks the unstrained state, A the peak in broken bonds, B the subsequent drop, and C and D strains of 0.15 and 0.3. Figure 8b,c show the side view at B (onset of bilayer water) and the close-up at C (nanoscale liquid-bridge stage) for 60-water systems without and with 40 H_2 molecules, respectively. Figure 8d,e illustrate tensile-loading trajectories at the five labeled points in the out-of-plane direction.

The disruption process begins with a sharp rise (O $\rightarrow$ A) in broken H-bonds, during which water inertia resists layer separation, increasing the water–surface oxygen distance, misaligning orientations, and destabilizing Na^+ hydration shells. This is followed by a sharp decrease (A $\rightarrow$ B) as water migrates vertically to form a bilayer (see Figure 8b,c, *x-z* view), reducing the average surface distance and reforming broken bonds. Finally, the process enters a plateau (B $\rightarrow$ D), where thin water films line the Mt surfaces and nanoscale liquid bridges form, resisting separation via surface tension and capillary suction forces (Figure 8c, perspective view). These stages are more pronounced in systems with lower water content, as a greater number of H-bonds are broken during the O $\rightarrow$ A stage, which means the three phases are more distinct in systems containing 60 water molecules than in those containing 240. In H_2-containing systems, once two thin water films coat the Mt sheets (point C), H_2 molecules accumulate in the central interlayer region (Figure 8c, close-up view). By comparison Figure 8b,c, close-up, it is clear that, acting as a non-wetting, nonpolar species unable to form H-bonds, H_2 forms a distinct phase that disrupts liquid bridges, weakens

interfacial forces, and lowers surface tension. As strain increases and the interlayer spacing expands, these bridges break, reducing stress. At point D, the Mt sheets are fully separated, with thin water layers covering them and H_2 concentrated at the nanopore center (Figure 8e).

The correlation between the stress–strain curve and the normalized number of broken H-bond diagram (Figure 8a) underscores the key role of H-bond disruption between Mt and water in controlling the system's mechanical behavior along the z-direction. H-bonds at the Mt interface act like microscopic springs, resisting vertical separation, and the applied stress primarily works to overcome them. Increasing the water content from 60 to 240 molecules significantly reduces the number of broken H-bonds, thereby lowering the UTS in the z-direction. As discussed above, increasing water reduces the ratio of the number of H-bonds formed between water and Mt molecules to the number of H-bonds formed between water molecules (Figure 1d), weakening surface adhesion and lowering the UTS in the z-direction (Figure 6c). This observation is consistent with the findings of Du et $al.$[68] on shear friction. Comparing systems without H_2 to those with 40 H_2 molecules shows a slight reduction in broken H-bonds at low water content but little effect at higher content, which is why H_2's influence is greater at low water contents, reducing UTS in the z-direction.
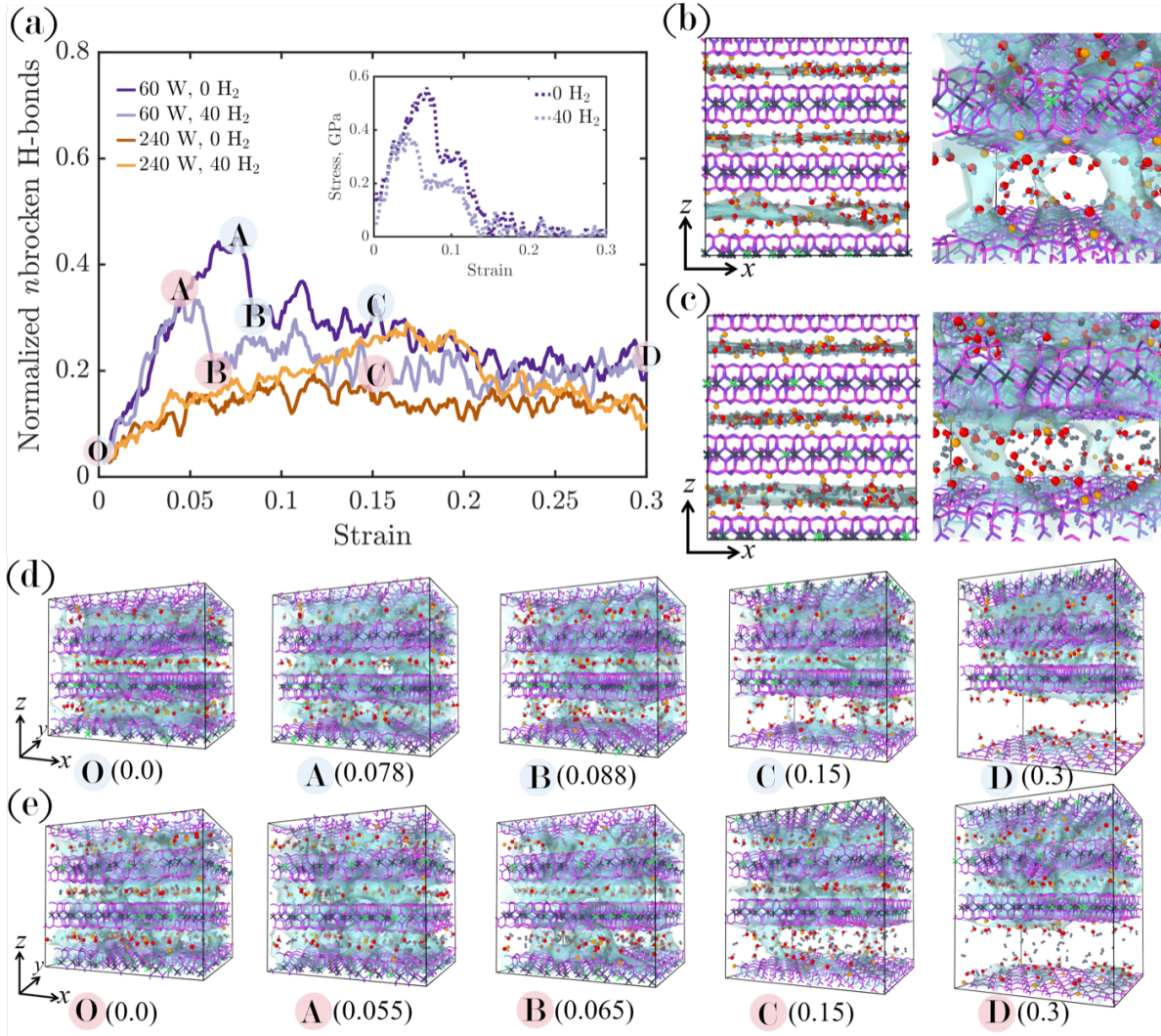
Figure 8: (a) Normalized number of broken H-bonds between Mt and interlayer water during z-direction tension for systems containing 60 and 240 water molecules, both without H_2 and with 40 H_2 molecules (inset shows the stress response for the 60-water system). (b, c) Side and close-up views at points B and C for the 60-water system without H_2 (b) and with 40 H_2 molecules (c). (d, e) Tensile deformation in the z-direction at the indicated points for the 60-water system without H_2 (d) and with 40 H_2 molecules (e).

Conclusions

This study provides critical insights into H_2-induced swelling and mechanical degradation in smectite clays, advancing the understanding of caprock integrity in subsurface H_2 storage. By quantifying H_2 effects on basal spacing, hydration energetics, and elastic–failure behavior, the work underscores the risks of diminished structural resilience and elevated leakage potential. The primary finding of this study are:

- In the presence of H_2, Mt swelling is markedly accelerated by altering the progression of hydration-state transitions. Under anhydrous conditions, H_2 expands the basal spacing from 9.7 Å to 10.4 Å (with addition of 40 interlayer H_2 molecules), accommodating gas molecules within the interlayer. In hydrated systems, H_2 reduces the amount of water required to trigger 1W and 2W transitions, thereby promoting earlier onset of swelling. While H_2 slightly deepens the hydration energy minimum, –53.77 kJ/mol, compared to -41.5 kJ/mol of internal energy of adopted water model, it also narrows the stability window of the crystalline swelling regime (1.875–3.75 H_2O/UC with H_2 vs. 1.875–5.0 H_2O/UC without H_2), indicating diminished structural resilience under variable hydration states.

- Above the solubility limit of H_2, gas-like plumes form, confined by water in the 1W state and evolving into cohesive clusters in the 2W state, thereby affecting interlayer cohesion and swelling dynamics. The asymmetric morphologies of these plumes, strongly influenced by isomorphic substitution sites in the octahedral sheet, reflect the interplay between local charge heterogeneity and nanoscale confinement. Structurally, these H_2 plumes enhance H-bonding within the interlayer water network at low hydration but disrupt it in the 2W state.

- Molecular interactions within the Mt interlayer show that H_2 repositions Na^+ ions and modulates water structure. In anhydrous Mt, H_2 shifts Na^+ closer to the clay surfaces, weakening ionic bonding, while in the 2W state it situates between the clay and cations,

enhancing hydration and interlayer expansion. At low hydration, H_2 disrupts water orientation, shifting dipole angles such that water molecules reorient with hydrogen atoms facing the slab surface, but its effect is minimal in stable 1W and 2W states due to strong water–water interactions.

- Mechanically, increasing the water and H_2 content in the Mt system reduces UTS and UCS in the x- and y-directions, along with lowering the in-plane stiffness coefficients, primarily due to the expansion of the basal spacing. The z-direction UTS and the out-of-plane stiffness coefficients are even more strongly affected by 50 to 75% for out-of-plane stiffness coefficients with 20 H_2, because the initial introduction of water and H_2 disrupts Na^+–Mt interactions. Both bulk modulus, K, and shear modulus, G, decrease with increasing water and H_2, driven by the combined effects of basal spacing expansion and disruption of the Na^+–Mt interface, whereas changes in Poisson's ratio, ν, does not follow a specific trend and fluctuates with water and H_2 content. These findings underscore the mechanical anisotropy of Mt and its critical role in modulating the effects of water and H_2.

- H-bonding at the Mt interface in non-dry systems governs the UTS in the z-direction. Additionally, H_2 disrupts nanoscale liquid bridges, facilitating the separation of Mt sheets. Under x- and y-directional tension, stress localizes in the T-sheet while bond breakage is more pronounced in the O-sheet. The stronger nanopore connectivity formed under x-direction tension is likely to increase the probability of H_2 leakage, in contrast to the weaker connectivity caused by platelet tilting in the y-direction, highlighting anisotropic failure modes that present critical vulnerabilities for H_2 storage in clay-rich caprock.

These findings challenge the applicability of CO_2-based models for H_2 storage, highlighting the need for tailored strategies to mitigate geo-mechanical instabilities in clay-rich caprock. The molecular mechanisms identified here, supported by comprehensive simulations, provide

a foundation for optimizing storage site selection and engineering solutions to improve long-term caprock sealing efficacy in geological H_2 storage systems. From a practical standpoint, this highlights the importance of characterizing clay mineralogy at the interlayer scale, for example, distinguishing between expandable smectite-rich systems and more stable illitic or chloritic phases, since swelling and mechanical softening are strongly governed by interlayer fluid content. Incorporating hydration state and cation composition, in addition to clay mineral type, into site-screening criteria would enhance predictions of caprock integrity under H_2 storage conditions. Meanwhile, it should be noted that our study considered an ideal Mt structure in terms of isomorphic substitutions, although such substitutions can significantly influence interlayer arrangements. Other clay minerals are therefore expected to behave differently depending on their specific structures. In addition, we focused on Na^+ as the interlayer cation, whereas other common cations such as K^+ and Ca^{2+} may alter the final arrangements due to their different charge densities and tendencies to form bonds with water molecules and basal surfaces. Further investigation is required to evaluate the impact of these factors.

CRediT authorship contribution statement

Mehdi Ghasemi: Conceptualization, Formal analysis, Investigation, Methodology, Software, Visualization, Data curation, Supervision, Writing − original draft, Writing − review & editing. **Mohamad Ali Ghafari**: Formal analysis, Methodology, Software, Validation, Data curation, Writing − original draft. **Masoud Babaei**: Conceptualization, Supervision, Writing − review & editing. **Valentina Erastova**: Conceptualization, Investigation, Supervision, Writing − review & editing.

Supporting Information Available

Supporting Information is available under the title *"Molecular Insights into Caprock Integrity of Subsurface Hydrogen Storage: Perspective on Hydrogen-Induced Swelling and Mechanical Response."* The Supporting Information includes: (1) methodology for computing elastic constants, (2) detailed description of analyses, (3) validation of the simulation procedure, and (4) additional results and discussion.

Acknowledgement

References

(1) Krevor, S.; De Coninck, H.; Gasda, S. E.; Ghaleigh, N. S.; de Gooyert, V.; Hajibeygi, H.; Juanes, R.; Neufeld, J.; Roberts, J. J.; Swennenhuis, F. Subsurface carbon dioxide and hydrogen storage for a sustainable energy future. Nature Reviews Earth & Environment **2023**, 4, 102–118.

(2) Heinemann, N.; Alcalde, J.; Miocic, J. M.; Hangx, S. J.; Kallmeyer, J.; Ostertag-Henning, C.; Hassanpouryouzband, A.; Thaysen, E. M.; Strobel, G. J.; Schmidt-Hattenberger, C.; others Enabling large-scale hydrogen storage in porous media–the scientific challenges. Energy & Environmental Science **2021**, 14, 853–864.

(3) Hassanpouryouzband, A.; Joonaki, E.; Edlmann, K.; Haszeldine, R. S. Offshore geological storage of hydrogen: is this our best option to achieve net-zero? ACS Energy Letters **2021**, 6, 2181–2186.

(4) Edlmann, K. Challenging perceptions of underground hydrogen storage. Nature Reviews Earth & Environment **2024**, 5, 478–480.

(5) Ghafari, M. A.; Ghasemi, M.; Niasar, V.; Babaei, M. Wetting preference of silica surfaces in the context of underground hydrogen storage: a molecular dynamics perspective. Langmuir **2024**, 40, 20559–20575.

(6) Ugarte, E. R.; Salehi, S. A review on well integrity issues for underground hydrogen storage. Journal of Energy Resources Technology **2022**, 144, 042001.

(7) Ghasemi, M.; Omrani, S.; Mahmoodpour, S.; Zhou, T. Molecular dynamics simulation of hydrogen diffusion in water-saturated clay minerals; implications for Underground Hydrogen Storage (UHS). International Journal of Hydrogen Energy **2022**, 47, 24871–24885.

(8) Kadoura, A.; Narayanan Nair, A. K.; Sun, S. Molecular dynamics simulations of carbon dioxide, methane, and their mixture in montmorillonite clay hydrates. The Journal of Physical Chemistry C **2016**, 120, 12517–12529.

(9) Cygan, R. T.; Romanov, V. N.; Myshakin, E. M. Molecular simulation of carbon dioxide capture by montmorillonite using an accurate and flexible force field. The Journal of Physical Chemistry C **2012**, 116, 13079–13091.

(10) Braid, H.; Taylor, K.; Hough, E.; Rochelle, C.; Niasar, V.; Ma, L. Hydrogen-induced mineral alteration: A review in the context of underground hydrogen storage (UHS) in saline aquifers. Earth-Science Reviews **2024**, 104975.

(11) Rahromostaqim, M.; Sahimi, M. Molecular dynamics simulation of hydration and swelling of mixed-layer clays in the presence of carbon dioxide. The Journal of Physical Chemistry C **2019**, 123, 4243–4255.

(12) Kahzadvand, K.; Ghasemi, M.; Yazaydin, A. O.; Babaei, M. Risk of H2 Leakage into caprock and the role of cushion gas as a barrier in H2 geo-storage: a molecular simulation study. The Journal of Physical Chemistry C **2024**, 128, 16161–16171.

(13) Sposito, G.; Skipper, N. T.; Sutton, R.; Park, S.-h.; Soper, A. K.; Greathouse, J. A. Surface geochemistry of the clay minerals. Proceedings of the National Academy of Sciences **1999**, 96, 3358–3364.

(14) Cygan, R. T.; Liang, J.-J.; Kalinichev, A. G. Molecular models of hydroxide, oxyhydroxide, and clay phases and the development of a general force field. The Journal of Physical Chemistry B **2004**, 108, 1255–1266.

(15) Ho, T. A.; Criscenti, L. J.; Greathouse, J. A. Revealing transition states during the hydration of clay minerals. The journal of physical chemistry letters **2019**, 10, 3704–3709.

(16) Mendel, N.; Sîretanu, D.; Sîretanu, I.; Brilman, D. W.; Mugele, F. Interlayer cation-controlled adsorption of carbon dioxide in anhydrous montmorillonite clay. The Journal of Physical Chemistry C **2021**, 125, 27159–27169.

(17) Hunvik, K. W. B.; Lima, R. J. d. S.; Kirch, A.; Loch, P.; Monceyron Røren, P.; Hoffmann Petersen, M.; Rudic, S.; Garcia Sakai, V.; Knudsen, K. D.; Rodrigues Miranda, C.; others Influence of CO2 on Nanoconfined Water in a clay Mineral. The Journal of Physical Chemistry C **2022**, 126, 17243–17254.

(18) Norrish, K. Crystalline swelling of montmorillonite: manner of swelling of montmorillonite. Nature **1954**, 173, 256–257.

(19) Collettini, C.; Niemeijer, A.; Viti, C.; Marone, C. Fault zone fabric and fault weakness. Nature **2009**, 462, 907–910.

(20) Busch, A.; Alles, S.; Gensterblum, Y.; Prinz, D.; Dewhurst, D. N.; Raven, M. D.; Stanjek, H.; Krooss, B. M. Carbon dioxide storage potential of shales. International journal of greenhouse gas control **2008**, 2, 297–308.

(21) Tetsuka, H.; Katayama, I.; Sakuma, H.; Tamura, K. Effects of humidity and interlayer cations on the frictional strength of montmorillonite. Earth, Planets and Space **2018**, 70, 1–9.

(22) Cygan, R. T.; Greathouse, J. A.; Kalinichev, A. G. Advances in clayff molecular simulation of layered and nanoporous materials and their aqueous interfaces. The Journal of Physical Chemistry C **2021**, 125, 17573–17589.

(23) Plimpton, S. Fast parallel algorithms for short-range molecular dynamics. Journal of computational physics **1995**, 117, 1–19.

(24) Mark, P.; Nilsson, L. Structure and dynamics of the TIP3P, SPC, and SPC/E water models at 298 K. The Journal of Physical Chemistry A **2001**, 105, 9954–9960.

(25) Yang, Q.; Zhong, C. Molecular simulation of adsorption and diffusion of hydrogen in metal- organic frameworks. The Journal of Physical Chemistry B **2005**, 109, 11862–11864.

(26) Gale, J. D.; Rohl, A. L. The general utility lattice program (GULP). Molecular Simulation **2003**, 29, 291–341.

(27) Voigt, W. Lehrbuch der kristallphysik:(mit ausschluss der kristalloptik); BG Teubner, 1910; Vol. 34.

(28) Ebrahimi, D.; Pellenq, R. J.-M.; Whittle, A. J. Nanoscale elastic properties of mont-morillonite upon water adsorption. Langmuir **2012**, 28, 16855–16863.

(29) Squire, D.; Holt, A.; Hoover, W. Isothermal elastic constants for argon. Theory and Monte Carlo calculations. Physica **1969**, 42, 388–397.

(30) Van Workum, K.; Yoshimoto, K.; de Pablo, J. J.; Douglas, J. F. Isothermal stress and elasticity tensors for ions and point dipoles using Ewald summations. Physical Review E—Statistical, Nonlinear, and Soft Matter Physics **2005**, 71, 061102.

(31) Parrinello, M.; Rahman, A. Strain fluctuations and elastic constants. The Journal of Chemical Physics **1982**, 76, 2662–2666.

(32) Van Workum, K.; de Pablo, J. J. Improved simulation method for the calculation of the elastic constants of crystalline and amorphous systems using strain fluctuations. Physical Review E **2003**, 67, 011505.

(33) Theodorou, D. N.; Suter, U. W. Atomistic modeling of mechanical properties of poly-meric glasses. Macromolecules **1986**, 19, 139–154.

(34) Mazo, M. A.; Manevitch, L. I.; Gusarova, E. B.; Berlin, A. A.; Balabaev, N. K.; Rutledge, G. C. Molecular dynamics simulation of thermomechanical properties of

montmorillonite crystal. II. Hydrated montmorillonite crystal. The Journal of Physical Chemistry C **2008**, 112, 17056–17062.

(35) Clavier, G.; Thompson, A. P. Computation of the thermal elastic constants for arbitrary manybody potentials in LAMMPS using the stress-fluctuation formalism. Comput. Phys. Commun. **2023**, 286, 108674.

(36) Clavier, G.; Desbiens, N.; Bourasseau, E.; Lachet, V.; Brusselle-Dupend, N.; Rousseau, B. Computation of elastic constants of solids using molecular simulation: comparison of constant volume and constant pressure ensemble methods. Molecular Simulation **2017**, 43, 1413–1422.

(37) Wei, P.; Zheng, Y.-Y.; Xiong, Y.; Zhou, S.; Al-Zaoari, K.; Zaoui, A. Effect of water content and structural anisotropy on tensile mechanical properties of montmorillonite using molecular dynamics. Applied Clay Science **2022**, 228, 106622.

(38) Wei, P.-C.; Zheng, Y.-Y.; Zaoui, A.; Yin, Z.-Y. Atomistic study on thermo-mechanical behavior and structural anisotropy of montmorillonite under triaxial tension and compression. Applied Clay Science **2023**, 233, 106817.

(39) Niu, W.; Zheng, Y.-Y.; Yin, Z.-Y.; Yao, C.; Wei, P. Multiscale mechanical behavior of hydrated expansive soil: Insights from experimental and MD study. Computers and Geotechnics **2025**, 181, 107129.

(40) Holmboe, M.; Bourg, I. C. Molecular dynamics simulations of water and sodium diffusion in smectite interlayer nanopores as a function of pore size and temperature. The Journal of Physical Chemistry C **2014**, 118, 1001–1013.

(41) Bérend, I.; Cases, J.-M.; François, M.; Uriot, J.-P.; Michot, L.; Masion, A.; Thomas, F. Mechanism of adsorption and desorption of water vapor by homoionic montmorillonites: 2. The Li+, Na+, K+, Rb+ and Cs+-exchanged forms. Clays and Clay Minerals **1995**, 43, 324–336.

(42) Li, Y.-C.; Wei, S.-J.; Xu, N.; He, Y. Internal forces within the layered structure of Na-montmorillonite hydrates: molecular dynamics simulation. The Journal of Physical Chemistry C **2020**, 124, 25557–25567.

(43) Teich-McGoldrick, S. L.; Greathouse, J. A.; Jove-Colon, C. F.; Cygan, R. T. Swelling properties of montmorillonite and beidellite clay minerals from molecular simulation: comparison of temperature, interlayer cation, and charge location effects. The Journal of Physical Chemistry C **2015**, 119, 20880–20891.

(44) Berendsen, H. J.; Grigera, J.-R.; Straatsma, T. P. The missing term in effective pair potentials. Journal of Physical Chemistry **1987**, 91, 6269–6271.

(45) Boek, E.; Coveney, P.; Skipper, N. Monte Carlo molecular modeling studies of hydrated Li-, Na-, and K-smectites: Understanding the role of potassium as a clay swelling inhibitor. Journal of the American Chemical Society **1995**, 117, 12608–12617.

(46) Pollak, H.; Degiacomi, M. T.; Erastova, V. Modeling Realistic Clay Systems with Clay-Code. Journal of Chemical Theory and Computation **2024**, 20, 9606–9617.

(47) Anderson, R. L.; Ratcliffe, I.; Greenwell, H.; Williams, P.; Cliffe, S.; Coveney, P. V. Clay swelling—a challenge in the oilfield. Earth-Science Reviews **2010**, 98, 201–216.

(48) Ho, T. A.; Jove-Colon, C. F.; Wang, Y. Low hydrogen solubility in clay interlayers limits gas loss in hydrogen geological storage. Sustainable Energy & Fuels **2023**, 7, 3232–3238.

(49) Van Rooijen, W.; Habibi, P.; Xu, K.; Dey, P.; Vlugt, T.; Hajibeygi, H.; Moultos, O. Interfacial tensions, solubilities, and transport properties of the H2/H2O/NaCl system: A molecular simulation study. Journal of Chemical & Engineering Data **2023**, 69, 307–319.

(50) Rahbari, A.; Brenkman, J.; Hens, R.; Ramdin, M.; Van Den Broeke, L. J.; Schoon, R.; Henkes, R.; Moultos, O. A.; Vlugt, T. J. Solubility of water in hydrogen at high pressures: a molecular simulation study. Journal of Chemical & Engineering Data **2019**, _64_, 4103–4115.

(51) Yen, T.-H.; Chen, Y.-L. Analysis of Gas Nanoclusters in Water Using All-Atom Molecular Dynamics. Langmuir **2022**, _38_, 13195–13205.

(52) Ortega, J. A.; Ulm, F.-J.; Abousleiman, Y. The effect of the nanogranular nature of shale on their poroelastic behavior. Acta Geotechnica **2007**, _2_, 155–182.

(53) Chen, B.; Evans, J. R. Elastic moduli of clay platelets. Scripta materialia **2006**, _54_, 1581–1585.

(54) Teich-McGoldrick, S. L.; Greathouse, J. A.; Cygan, R. T. Molecular dynamics simulations of structural and mechanical properties of muscovite: pressure and temperature effects. The Journal of Physical Chemistry C **2012**, _116_, 15099–15107.

(55) Militzer, B.; Wenk, H.-R.; Stackhouse, S.; Stixrude, L. First-principles calculation of the elastic moduli of sheet silicates and their application to shale anisotropy. American Mineralogist **2011**, _96_, 125–137.

(56) McNeil, L.; Grimsditch, M. Elastic moduli of muscovite mica. Journal of Physics: Condensed Matter **1993**, _5_, 1681.

(57) Zartman, G. D.; Liu, H.; Akdim, B.; Pachter, R.; Heinz, H. Nanoscale tensile, shear, and failure properties of layered silicates as a function of cation density and stress. The Journal of Physical Chemistry C **2010**, _114_, 1763–1772.

(58) Zhang, W.; Hu, H.; Li, X.; Fang, Z. Interplay of montmorillonite–H2O–scCO2 system between mechanical behavior and adsorption: molecular dynamics. The Journal of Physical Chemistry C **2015**, _119_, 21959–21968.

(59) Zhang, W. N.; Hu, H. X.; Li, X. C.; Fang, Z. M. Evolutions in the elastic constants of Ca-montmorillonites with H2O/CO2 mixture under supercritical carbon dioxide conditions. The Journal of Physical Chemistry C **2017**, 121, 2702–2710.

(60) Carrier, B.; Vandamme, M.; Pellenq, R. J.-M.; Van Damme, H. Elastic properties of swelling clay particles at finite temperature upon hydration. The Journal of Physical Chemistry C **2014**, 118, 8933–8943.

(61) Li, B.; Li, C.; Gui, Y.; Zhan, H.; Gu, Y.; Yu, M.; Rowe, R. K. Understanding structural anisotropy and mechanical properties of Na-montmorillonite with crystalline swelling and uniaxial deformation under different hydration degrees. Computers and Geotechnics **2024**, 169, 106200.

(62) Li, D.; Li, G.; Bai, Z.; Han, Z.; Lu, W. Deformation and failure processes of Na-montmorillonite under uniaxial compressive strain condition via molecular dynamic method. Materials Today Communications **2023**, 35, 106132.

(63) Zhang, C.-L.; Armand, G.; Conil, N.; Laurich, B. Investigation on anisotropy of mechanical properties of Callovo-Oxfordian claystone. Engineering Geology **2019**, 251, 128–145.

(64) Zhang, Y.; Gao, S.; Du, X.; Chen, M.; Jin, Y. Molecular dynamics simulation of strength weakening mechanism of deep shale. Journal of Petroleum Science and Engineering **2019**, 181, 106123.

(65) Zhao, H.; Cui, H.; Jiang, S.; Awadalseed, W.; Guo, J.; Yang, W.; Kang, X. Tensile and compressive behavior of Na-, K-, Ca-Montmorillonite and temperature effects. Chemical Physics **2023**, 569, 111855.

(66) Yang, H.; He, M.; Lu, C.; Gong, W. Deformation and failure processes of kaolinite under tension: Insights from molecular dynamics simulations. Science China Physics, Mechanics & Astronomy **2019**, 62, 64612.

(67) Rastogi, A.; Ghosh, A. K.; Suresh, S. Hydrogen bond interactions between water molecules in bulk liquid, near electrode surfaces and around ions. Thermodynamics-Physical chemistry of aqueous systems **2011**, 351–364.

(68) Du, J.; Zhou, A.; Shen, S.-L.; Lin, X.; Kodikara, J. Influence of hydration film on the frictional behavior of montmorillonite: Insights into microscopic mechanics of layered minerals. The Journal of Physical Chemistry C **2024**, 128, 14407–14419.